# Systematic single-folding optical potential for $^6$Li and $^7$Li based on KD02 potentials

Yazhou Lu, Jin Lei,[*] and Zhongzhou Ren

*School of Physics Science and Engineering, Tongji University, Shanghai 200092, China*

In the present research, we utilized the single-folding model to develop a systematical optical potential for $^6$Li and $^7$Li, employing the nucleon-nucleus global potentials introduced by Koning and Delaroche (KD02). We analyzed the elastic scattering angular distributions of $^6$Li and $^7$Li on targets with mass numbers ranging from 24 to 209 using the single-folding potential. Incident energies between 5 and 55 MeV/nucleon were considered. The real part of the single-folding model potential was renormalized with one free parameter, while leaving its imaginary part unchanged. The resulting renormalization factors of the single-folding model potentials show consistent systematics. Our approach effectively reproduced the elastic scattering and reaction cross sections of the targets in our current study. In addition, we also compared the prediction abilities of our systematic optical potentials with those of others.

## I. INTRODUCTION

The central objective of nuclear physics is to understand nuclear structures through nuclear reactions. Optical model potential (OMP), which is widely utilized in studying various nuclear reactions, including elastic scattering, inelastic scattering, transfer, and breakup reactions [1–3], is a crucial input for theoretical modeling of nuclear reactions [4–6].

In the optical model, the scattering wave function $\chi^{(+)}$ approximates the elastic component of $\xi_0^{(+)}$ of the many-body wave function of both the projectile and target, assuming that both are at their ground states. In simpler terms, $|\chi^{(+)}(\vec{r})|^2$ is an estimation of the probability of the two nuclei, $a + A$ to be positioned in their ground states and separated by $\vec{r}$.

In many cases, the OMP is determined by fitting an analytical form, such as the Woods-Saxon form, to experimental data. However, there is a lack of relevant experimental data when dealing with exotic nuclei far from the beta stability. In such cases, systematic OMP provides significant value and allows for the prediction of nucleon-nucleus or nucleus-nucleus potentials when no experimental data are available. Seeking a systematic optical potential for light particles has been a longstanding goal in nuclear physics research. To this end, numerous studies have focused on determining the optical parameters for proton, neutron, deuteron, triton, and $\alpha$ particles [7–15]. However, describing the interaction of the weakly bound projectiles with target nuclei across a range of incident energies and reaction systems presents unique challenges. To address this challenge, Cook proposed a global OMP for $^6$Li and $^7$Li that characterizes both the real and imaginary components of the potential using the Woods-Saxon form [16], which was later improved by Zagatto *et al.* [17]. Xu *et al.* proposed a more globally applicable phenomenological

OMP for the same systems in 2018 [18,19]. Additionally, global optical potentials for $^6$Li and $^7$Li have been developed using the single-folding model with a range of target masses and large energy. These optical potentials are successful in reproducing observed scattering data by mimicking the behavior of the wave function outside the interaction region, $\chi^{(+)}(\vec{r}) \approx \xi_0^{(+)}(\vec{r})$ when $r > R_{\text{int}}$. However, there are ambiguities in their use in reaction calculations, such as the distorted wave method, since the results of these depend on the wave function for $r < R_{\text{int}}$.

In the distorted wave method, systematic ambiguities can be reduced for $r < R_{\text{int}}$ if all the potentials used in the calculations are based on the same interactions. This is exemplified in the inclusive breakup reaction $a + A \rightarrow b + B^*$, where $B^*$ represents any possible state of the $x + A$ system. When considering this inclusive breakup reaction in the distorted wave Born approximation (DWBA) form and comparing it with the continuum-discretized coupled-channels (CDCC) form, the selection of the optical potential for $a + A$ becomes crucial [20]. In such scenarios, employing single-folding potentials offers several advantages. It helps mitigate systematic errors, especially those originating from the inner region of the scattering wave function of $a + A$ as required by DWBA. This is particularly pertinent in the case of the effective interactions utilized in the CDCC calculation, which are derived from the same single folding potential. The inner segment of the wave function cannot be determined experimentally, yet its influence on the computation of final observables is considerable. This effect becomes particularly significant when the surface approximation is invalid [21].

We applied the single-folding model in this study to generate new systematic optical potentials. These potentials were derived from the Koning and Delaroche (KD02 [11]) global nucleon-nucleus optical potential, which is widely used in reaction calculations. Incorporating this new systematic optical potential consistently into the required effective interactions for reaction calculations can significantly reduce systematic

---

*jinl@tongji.edu.cn

ambiguities. In this study, we employ the $^{6,7}$Li-induced reactions as examples to investigate the potential application of the single-folding potential. In general, this model can be implemented for various types of projectiles, thereby enabling the derivation of a systematic potential in reaction calculations. This single folding potential involves folding the nucleon-nucleus interaction with the density distribution of the projectile to obtain the single-folding model potential. This potential is then renormalized to obtain the effective interaction that describes the nucleus-nucleus elastic scattering and reaction cross sections. The systematic nature of the obtained normalization factors is of significant relevance for nuclear physics [22].

In previous studies, renormalization was made to both the real and imaginary parts of the single-folding model potential [14,23]. However, our investigation showed that modifying the imaginary part of the potential did not lead to a noteworthy improvement in the systematic optical potential. This finding can also be justified based on the CDCC calculation reported in Ref. [24]. In this reference, the authors assert that the coupled channel effect of the breakup channels is accurately accounted for in the optical potential calculation. They achieve this by reducing the real part of the double folding potential strength by a factor of two, with minimal adjustments required for the imaginary potential. Therefore, we focused on scrutinizing the systematics of the real part of the single-folding potential that implies determining one free parameter by fitting nuclear scattering data. The quality of fitting is often a tradeoff between the number of parameters and fitting quality; too few parameters result in poor fitting quality, whereas too many parameters lead to unsystematic potentials. We were able to obtain a systematic optical potential, which has similar predictive capabilities to previous works, with one less parameter used. Additionally, we investigated the dependence of these renormalization factors on the ratio of incident energy in the center of mass (c.m) frame to the Coulomb barrier, as nucleus-nucleus scattering is largely influenced by the Coulomb potential [25–27].

The universal applicability of the KD02 optical potential across a broad range of energy and target mass numbers makes our systematic optical potential suitable for studying nuclear reactions over a wide range of energies, spanning from a few to several hundreds of MeV and for target mass numbers from 24 to 209. The KD02 optical potential is widely used in theoretical calculations and has demonstrated good performance in predicting nucleon scattering. Therefore, the renormalization of the single-folding model potential primarily results from the compound effect of the nucleus.

This paper is organized as follows. In Sec. II, we provide an overview of the single-folding model. In Sec. III, we present the methods for conducting optical model analysis on experimental data and determining the systematic optical potential renormalization factors for $^6$Li and $^7$Li. To evaluate the performance of our systematic optical potential, we compare the angular distributions of elastic scattering and reaction cross sections with optical model calculations in Sec. IV. In this section, we also compare our findings with other phenomenological optical potentials. Lastly, we summarize our results and draw conclusions in Sec. V.
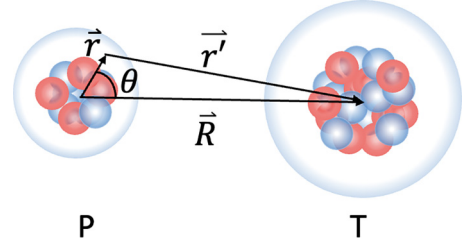


FIG. 1. Coordinates used in single-folding model calculations.

## II. THE SINGLE-FOLDING MODEL POTENTIAL

In this section, we present a concise overview of the single-folding model. The potential given by this model is expressed as

$$U_{SF}(|\boldsymbol{R}|, E_{\text{lab}}) = \sum_{i=n,p} \int \rho_i(|\boldsymbol{r}|) \mathcal{U}_{iT}(|\boldsymbol{r}'|, E_i) d\boldsymbol{r}, \quad (1)$$

where $\boldsymbol{R}$ is the vector between the projectile and the target, as depicted in Fig. 1. $\rho_i(|\boldsymbol{r}|)$ is the density of nucleons ($i = p$ for proton and $i = n$ for neutron) in the projectile at position $\boldsymbol{r}$ from its center of mass. The term $\mathcal{U}_{iT}(|\boldsymbol{r}'|, E_i)$ is the optical potential for the nucleon-target system, which is dependent on the modulus of vector $\boldsymbol{r}'$ and the incident energy per nucleon of the projectiles represented by $E_i$, where $\boldsymbol{r}' = \boldsymbol{R} + \boldsymbol{r}$, and $E_i = E_{\text{lab}}/A_p$. Here, $A_p$ is the mass number of the projectile.

The density of nucleons, $\rho_i$, in the projectile was obtained through relativistic mean field calculations using DD-ME2 interactions [28]. For nucleon-nucleus optical potential, $\mathcal{U}_{iT}$, we chose the KD02 optical potential [11] in our study. The KD02 optical potential consists of volume, surface, and spin-orbital terms, thus offering a reliable method of describing nucleon-nucleus scattering. In this study, we only analyzed the angular distributions for elastic scattering and reaction cross sections, which are often considered insensitive to the spin-orbital part [29]. Consequently, the spin-orbital part of the KD02 potential is not included in our calculation. Then the optical potential, $\mathcal{U}_{iT}$, can be expressed as

$$\mathcal{U}_{iT}(r', E_i) = -\mathcal{V}_V(r', E_i) - i\mathcal{W}_V(r', E_i)$$
$$- i\mathcal{W}_D(r', E_i), \quad (2)$$

where $r' = |\boldsymbol{r}'|$, which is the distance between a nucleon and the target. $\mathcal{V}_V$ and $\mathcal{W}_V$ are the real and imaginary components of the volume term, respectively. The surface component is captured by $\mathcal{W}_D$. All components are expressed by energy-dependent well depths, $V_V$, $W_V$, and $W_D$, and energy-independent radial parts $f$, namely,

$$\mathcal{V}_V(r', E_i) = V_V(E_i) f(r', R_V, a_V),$$
$$\mathcal{W}_V(r', E_i) = W_V(E_i) f(r', R_V, a_V),$$
$$\mathcal{W}_D(r', E_i) = -4a_D W_D(E_i) \frac{d}{dr'} f(r', R_D, a_D). \quad (3)$$

The form factor $f(r', R_i, a_i)$ takes Woods-Saxon shape, which is given by

$$f(r', R_i, a_i) = \frac{1}{1 + \exp\left[\frac{r' - R_i}{a_i}\right]}, \quad (4)$$

where $R_i$, which is determined by the atomic mass number $A_T$ of the target nucleus, is given by $R_i = r_i A_T^{1/3}$. $r_i$ is the radius parameter. The symbol $a_i$ denotes the diffuseness parameter. All necessary information regarding the calculations of the depths, $V_V$, $W_V$, and $W_D$, as well as their corresponding geometry parameters, $r_i$ and $a_i$, are available in Ref. [11].

In the single-folding model approach, we derive the nuclear portion of the nucleus-nucleus potential by utilizing Eq. (1). To acquire the overall potential, we must consider the inclusion of the Coulomb potential. Additionally, we must renormalize the single-folding model potential to elucidate the nucleus-nucleus elastic scattering and the reaction cross sections owed to the composite nature of the projectile nucleus [30]. Consequently, the complete nucleus-nucleus potential, in our single-folding model approach, adopts the following form:

$$U(R, E_{\text{lab}}) = N_r \text{Re}[U_{SF}(R, E_{\text{lab}})]$$
$$+ i\text{Im}[U_{SF}(R, E_{\text{lab}})] + V_C(R), \quad (5)$$

where $N_r$ represents the renormalization factors for the real part of the single-folding potential. The Coulomb potential, $V_C$, is calculated in the standard way using a radius $R_C = r_C(A_P^{1/3} + A_T^{1/3})$. Throughout our study, we set $r_C = 1.2$ fm. In comparison to halo nucleus induced reactions, breakup effects in the Li-induced reactions we studied are weaker. This study aims to investigate the elastic scattering of $^{6,7}$Li, where we expect less pronounced breakup effects. However, if necessary, the additional surface imaginary interaction discussed in Ref. [31] can be used to add the breakup effects. Only the real part of the single folding potential is renormalized in this study. The change in the real part is primarily caused by the dynamic polarization potential resulting from the electric field of the target polarizing the projectile. This Coulomb dynamic polarization potential can be complex, where the imaginary part reflects the effects of the breakup. Our focus is on the $^{6,7}$Li induced reaction, where the breakup effects are not as strong as in halo nucleus induced reactions. In addition, the renormalization of the real part of the single folding potential is consistent with the results obtained in Ref. [32]. Reference [32] also normalizes the real part of $\alpha + ^{208}$Pb and $t + ^{208}$Pb potentials by a factor of 0.6 in performing the CDCC calculation, which reproduces experimental data.

## III. ANALYSIS OF $^6$Li and $^7$Li SYSTEMATIC OPTICAL POTENTIAL

### A. Procedures of data analysis

This subsection aims to determine the optimal normalization factors by fitting experimental data of nucleus-nucleus elastic scattering and establish their energy dependence. Therefore, in the first step, we gathered the experimental data of elastic scattering angular distribution of $^6$Li and $^7$Li. The relevant experimental data and their references for $^6$Li and $^7$Li are listed in Tables I and II, respectively.

This study concentrates on targets with atomic mass numbers within the range of 24 to 209, and incident projectile energy ranging from 5 to 55 MeV/nucleon. We retrieved the experimental data from the EXFOR/CSISRS nuclear reaction

TABLE I. The experimental data analyzed in this work, along with their references, the ratio of the incident energy in the center of mass coordinate system to the Coulomb barrier, and the resulting renormalization factors for $^6$Li are presented.

| Target | $E_{\text{lab}}$/MeV | $E_r$ | $N_r$ | Ref. |
|---|---|---|---|---|
| $^{24}$Mg | 72.7 | 9.561 | 0.416 | [38] |
| | 240.0 | 31.563 | 0.597 | [40] |
| $^{25}$Mg | 34.0 | 4.543 | 0.327 | [42] |
| $^{26}$Mg | 34.0 | 4.613 | 0.413 | [42] |
| | 36.0 | 4.884 | 0.418 | [43] |
| | 72.7 | 9.863 | 0.500 | [38] |
| $^{27}$Al | 34.0 | 4.286 | 0.330 | [42] |
| $^{28}$Si | 34.0 | 4.007 | 0.457 | [45] |
| | 60.0 | 7.071 | 0.394 | [47] |
| | 75.0 | 8.839 | 0.425 | [47] |
| | 90.0 | 10.606 | 0.385 | [47] |
| | 99.0 | 11.667 | 0.434 | [34] |
| | 210.0 | 24.748 | 0.648 | [52] |
| | 240.0 | 28.284 | 0.629 | [40] |
| | 318.0 | 37.476 | 0.711 | [52] |
| $^{39}$K | 34.0 | 3.226 | 0.399 | [53] |
| | 37.0 | 3.510 | 0.417 | [53] |
| $^{40}$Ca | 99.0 | 8.957 | 0.477 | [34] |
| | 156.0 | 14.114 | 0.533 | [35] |
| | 210.0 | 19.000 | 0.561 | [52] |
| | 240.0 | 21.714 | 0.546 | [54] |
| $^{58}$Ni | 34.0 | 2.400 | 0.334 | [55] |
| | 73.7 | 5.202 | 0.404 | [49] |
| | 90.0 | 6.353 | 0.523 | [48] |
| | 99.0 | 6.988 | 0.406 | [34] |
| | 240.0 | 16.941 | 0.521 | [54] |
| $^{89}$Y | 60.0 | 3.351 | 0.367 | [57] |
| $^{90}$Zr | 34.0 | 1.854 | 0.282 | [39] |
| | 60.0 | 3.271 | 0.273 | [57] |
| | 70.0 | 3.817 | 0.373 | [41] |
| | 73.7 | 4.018 | 0.377 | [49] |
| | 99.0 | 5.398 | 0.356 | [34] |
| | 156.0 | 8.505 | 0.459 | [35] |
| | 210.0 | 11.450 | 0.341 | [52] |
| | 240.0 | 13.085 | 0.409 | [54] |
| $^{91}$Zr | 34.0 | 1.860 | 0.333 | [39] |
| $^{92}$Zr | 70.0 | 3.840 | 0.450 | [41] |
| $^{94}$Zr | 70.0 | 3.864 | 0.459 | [41] |
| $^{96}$Zr | 70.0 | 3.886 | 0.463 | [41] |
| $^{112}$Sn | 35.0 | 1.594 | 0.436 | [44] |
| $^{116}$Sn | 35.0 | 1.609 | 0.547 | [44] |
| | 240.0 | 11.036 | 0.505 | [44] |
| $^{120}$Sn | 44.0 | 2.042 | 0.239 | [46] |
| | 90.0 | 4.177 | 0.651 | [48] |
| $^{124}$Sn | 73.7 | 3.452 | 0.389 | [49] |
| $^{208}$Pb | 31.0 | 0.981 | 0.472 | [50] |
| | 33.0 | 1.044 | 0.398 | [51] |
| | 35.0 | 1.107 | 0.349 | [50] |
| | 39.0 | 1.234 | 0.416 | [51] |
| | 43.0 | 1.360 | 0.153 | [50] |
| | 46.0 | 1.455 | 0.129 | [50] |
| | 73.7 | 2.332 | 0.351 | [49] |
| | 90.0 | 2.847 | 0.558 | [48] |
| | 99.0 | 3.132 | 0.328 | [34] |
| | 156.0 | 4.936 | 0.406 | [35] |

TABLE I. (*Continued.*)

| Target | $E_{\text{lab}}/\text{MeV}$ | $E_r$ | $N_r$ | Ref. |
|--------|------|------|------|------|
| | 210.0 | 6.644 | 0.424 | [52] |
| $^{209}$Bi | 32.0 | 1.001 | 0.416 | [56] |
| | 34.0 | 1.063 | 0.297 | [56] |
| | 36.0 | 1.126 | 0.339 | [56] |
| | 38.0 | 1.188 | 0.292 | [56] |
| | 40.0 | 1.251 | 0.279 | [56] |
| | 44.0 | 1.376 | 0.372 | [56] |
| | 50.0 | 1.564 | 0.299 | [56] |

database [33], with the exception of $^6$Li at 99 and 156 MeV, and $^7$Li at 52 and 88.7 MeV, which we extracted from figures in Refs. [34–37], respectively. We utilized uncertainties provided for experimental data points in our analysis. For consistency, in cases where uncertainties were not provided, we used uniform uncertainties of 5% for the data points. We employed the traditional minimum $\chi^2/N$ ($N$ being the number of experimental data points) method to fit the experimental data, and to determine the potential renormalization factors, $N_r$, for each data set. We used SFRESCO, a computer code that combines FRESCO [64] and the search algorithm MINUIT

TABLE II. The experimental data analyzed in this work, along with their references, the ratio of the incident energy in the center of mass coordinate system to the Coulomb barrier, and the resulting renormalization factors for $^7$Li are presented.

| Target | $E_{\text{lab}}/\text{MeV}$ | $E_r$ | $N_r$ | Ref. |
|--------|------|------|------|------|
| $^{24}$Mg | 88.0 | 11.602 | 0.430 | [37] |
| $^{26}$Mg | 88.0 | 11.987 | 0.462 | [37] |
| $^{28}$Si | 36.0 | 4.234 | 0.408 | [43] |
| | 350.0 | 41.164 | 0.676 | [58] |
| $^{40}$Ca | 34.0 | 3.091 | 0.373 | [59] |
| | 88.0 | 8.063 | 0.262 | [37] |
| $^{44}$Ca | 34.0 | 3.193 | 0.437 | [59] |
| $^{48}$Ca | 34.0 | 3.286 | 0.413 | [59] |
| | 88.0 | 8.573 | 0.269 | [37] |
| $^{54}$Fe | 36.0 | 2.719 | 0.348 | [59] |
| | 42.0 | 3.172 | 0.353 | [59] |
| | 48.0 | 3.625 | 0.391 | [59] |
| $^{56}$Fe | 34.0 | 2.597 | 0.380 | [59] |
| $^{58}$Ni | 34.0 | 2.626 | 0.353 | [59] |
| | 42.0 | 3.244 | 0.302 | [60] |
| $^{60}$Ni | 34.0 | 2.449 | 0.389 | [59] |
| $^{89}$Y | 60.0 | 3.397 | 0.248 | [57] |
| $^{90}$Zr | 34.0 | 1.879 | 0.328 | [59] |
| $^{116}$Sn | 35.0 | 1.633 | 0.398 | [61] |
| $^{118}$Sn | 48.0 | 2.251 | 0.383 | [16] |
| $^{142}$Nd | 52.0 | 2.109 | 0.416 | [36] |
| $^{144}$Sm | 35.0 | 1.375 | 0.324 | [62] |
| | 40.8 | 1.603 | 0.255 | [62] |
| | 52.0 | 2.044 | 0.426 | [36] |
| $^{208}$Pb | 33.0 | 1.061 | 0.249 | [51] |
| | 37.55 | 1.208 | 0.372 | [63] |
| | 39.0 | 1.254 | 0.526 | [51] |
| | 42.55 | 1.368 | 0.365 | [63] |
| | 52.0 | 1.672 | 0.449 | [36] |
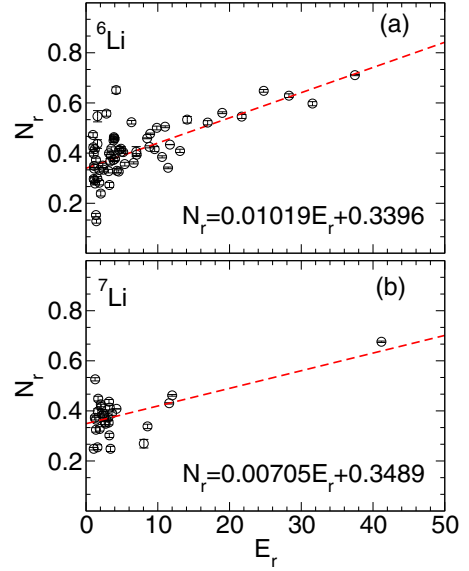


FIG. 2. (a) and (b) present the renormalization factors, $N_r$, as a function of the ratio of the incident energy in the c.m. frame to Coulomb barrier, denoted as $E_r$, for $^6$Li and $^7$Li, respectively. The symbols represent the fitted renormalization factors, $N_r$. The dashed line indicates the fitted linear function.

[65], to fit optical potentials. We enforced the maximum and minimum values of $N_r$ at 1.0 and 0.01, respectively, to prevent unrealistically large or small values. The resulting fitted values of $N_r$ for $^6$Li and $^7$Li are recorded in Tables I and II, respectively.

We utilized the fitted $N_r$ values that yielded optimal matches for every experimental angular distribution to analyze the relationship between these factors and the projectile bombarding energies. Due to the different Coulomb barrier energies, the most effective method for comparison is to represent the reaction energy as a ratio of incident energy in the center-of-mass coordinate system to the Coulomb barrier, where a ratio less than 1 signifies bombarding energies below the barrier, while a ratio greater than 1 indicates reactions occurring at energies above the barrier. To accomplish this, we introduced the variable $E_r$, defined as

$$E_r = E_{\text{c.m.}}/V_{CB}, \tag{6}$$

where $E_{\text{c.m.}}$ represents the incident energy of the projectile in the c.m. frame, while $V_{CB}$ denotes the Coulomb barrier. Notably, $E_r$ is a dimensionless value. Details on calculating $V_{CB}$ are available in Refs. [27].

In Fig. 2, we presented the values of $N_r$ for $^6$Li (a) and $^7$Li (b), estimated through circles symbols, as a function of $E_r$. As illustrated, there is a strong linear correlation between $N_r$ and $E_r$ for $^6$Li and $^7$Li, as long as the values of $E_r$ fall within the 1 to 50 range. Based on this observation, a linear function was utilized to estimate the $N_r$ values of $^6$Li and $^7$Li, as given by

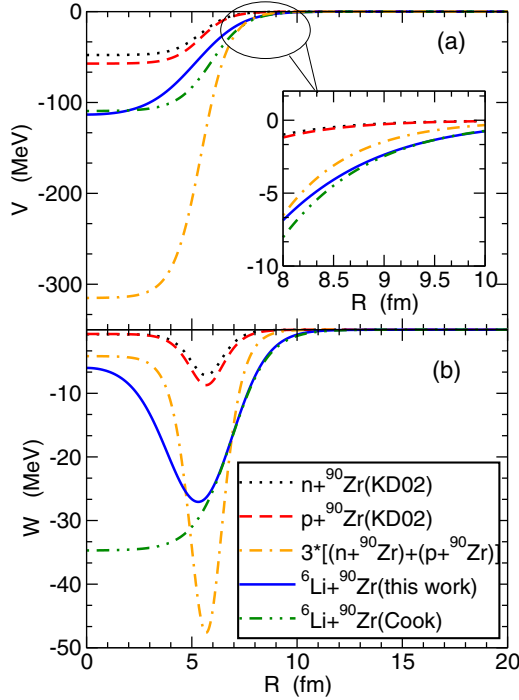$$N_r(^6\text{Li}) = 0.01019E_r + 0.3396, \tag{7}$$

$$N_r(^7\text{Li}) = 0.00705E_r + 0.3489. \tag{8}$$

FIG. 3. The real and imaginary parts of the optical potential for the $^6$Li $+$ $^{90}$Zr system, $n + ^{90}$Zr system, and $p + ^{90}$Zr system at an incident energy of 10 MeV/u. The neutron optical potential of KD02 is represented by the dotted line, while the proton optical potential is represented by the dashed line. The result of directly summing the three neutron optical potentials and three proton optical potentials is indicated by the dot-dashed line. Our current optical potential for $^6$Li $+$ $^{90}$Zr, which is the systematic optical potential with the real part adjusted using Eq. (8), is represented by the solid line. Cook's optical potential is indicated by the dot-dot-dashed line.

The resulting fit is incorporated as dashed lines within Fig. 2. While much of the provided experimental data for $^7$Li had incident energies below 88.7 MeV, the scattering $^{28}$Si at 350 MeV depicted an ascent in $N_r$ as $E_r$ increased. To account for this effect, we assumed that this element possesses a relationship comparable to that observed in $^6$Li, and thus we incorporated a linear function to estimate the $N_r$ values of $^7$Li according to Eq. (9). By adopting linear functions, we intend to capture the energy dependence of the renormalization factors without specific physical implications. Our findings indicate that the energy dependence of $N_r$ corresponds qualitatively to the observations described in Ref. [23]. We note that the parameters in Eqs. (8) and (9) enhance in accuracy as the experimental data set becomes more extensive. As there might be a lack of experimental data for $^7$Li at high energies, additional experimental data could necessitate significant modifications in the parameters of Eq. (9).

### B. Shapes and volume integrals of present potential

Figure 3 displays the current single-folding [i.e., the real part of the optical potential obtained through Eq. (8)] and Cook's optical potentials for the $^6$Li $+$ $^{90}$Zr system at 10 MeV/u represented by solid and dot-dot-dashed lines,

respectively. The proton and neutron optical potentials of KD02 are also plotted as dotted and dashed lines, respectively. Note that $^6$Li contains three protons and three neutrons. To illustrate the effects of their combined potentials, we show the sum of the three neutron optical potentials and the three proton optical potentials with a dot-dashed line on the same figure.

The results in panel (a) of Fig. 3 reveal that the real part of the current systematic optical potential is significantly lower than the sum of the real parts of the three neutron and three proton potentials. However, compared to Cook's systematic optical potential, the real part of the current systematic optical potential has a similar magnitude, although there are slight differences in their shape. Nevertheless, most heavy-ion scattering data are only sensitive to the potential tail in the vicinity of the strong absorption radius, which is usually about $R_{\text{str}} = 1.5(A_P^{1/3} + A_T^{1/3})$ fm [66,67]. Therefore, a subplot is included in Fig. 3(a) to provide a more detailed view of this region. We observe that the real part of the current systematic optical potential is similar to Cook's systematic optical potential when $R \geqslant 8.5$ fm.

Figure 3(b) shows that the imaginary part of the current systematic optical potential is nearly identical to Cook's systematic optical potential when $R \geqslant 5$ fm. However, the results obtained by directly adding the imaginary part of the three neutron potentials and the three proton potentials are significantly different from the current single-folding potential, as depicted in Fig. 3(b). This difference indicates that the distribution of nucleons within the projectile has a significant impact on nucleus-nucleus scattering.

The volume integrals per nucleon of OMP have significant implications for modeling nuclear interactions. Particularly in the study of interactions between light heavy-ions with targets [68]. In prior research, Greenlees *et al.* [69] demonstrated that the volume integral per nucleon's real part can attain high accuracy based entirely on cross-sectional data. Additionally, other studies [70,71], demonstrated that the imaginary part of the volume integral per nucleon was also well determined by the data. The real parts of the volume integrals per nucleon ($J_r$) and imaginary parts of the volume integrals per nucleon ($J_i$) of the OMP are defined as

$$J_r(E) = \frac{4\pi}{A_P A_T} \int N_r \text{Re}[U_{SF}(R, E)]R^2 dR, \qquad (9)$$

$$J_i(E) = \frac{4\pi}{A_P A_T} \int \text{Im}[U_{SF}(R, E)]R^2 dR, \qquad (10)$$

where $A_P$ and $A_T$ represent the mass numbers of the projectile and target, respectively.

Figure 4 presents the real part of the volume integrals per nucleon of the optical potentials as a function of target mass number. Panels (a), (b), and (c) represent incident energies of 5 MeV/u, 20 MeV/u, and 40 MeV/u, respectively. The cross and plus symbols represent the real part of the volume integrals per nucleon of our current optical potential for $^6$Li and $^7$Li, respectively. The solid and dot-dashed lines represent the real part of the volume integrals per nucleon of Cook's optical potential for $^6$Li and $^7$Li, respectively. The same quantities for the proton (dot line) and neutron (dashed line) are also displayed at the same energy per nucleon. First, the behavior
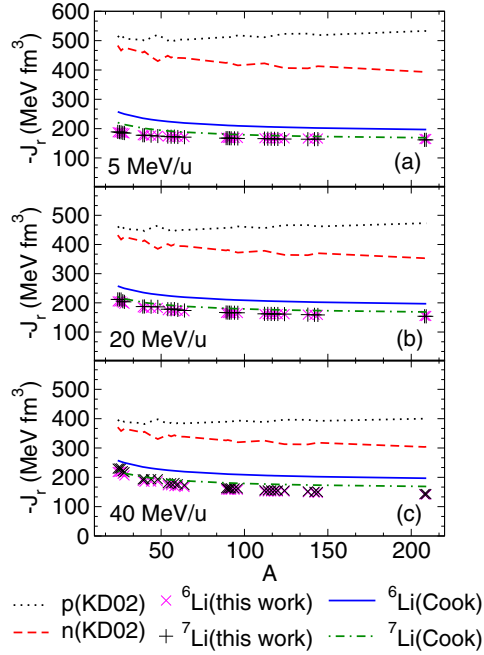
FIG. 4. Real part of the volume integrals per nucleon of different optical potential as a function of target mass number. (a), (b), and (c) represent incident energy of 5 MeV/u, 20 MeV/u, and 40 MeV/u, respectively. The dotted line represents the volume integrals per nucleon derived by the nucleon optical potential of KD02, while the dashed line represents the volume integrals per nucleon derived by the proton optical potential of KD02. The present optical potentials for $^6$Li and $^7$Li are demonstrated by the plus symbols and cross symbols, respectively. Cook's optical potential for $^6$Li and $^7$Li are represented by the solid and dot-dashed lines, respectively.
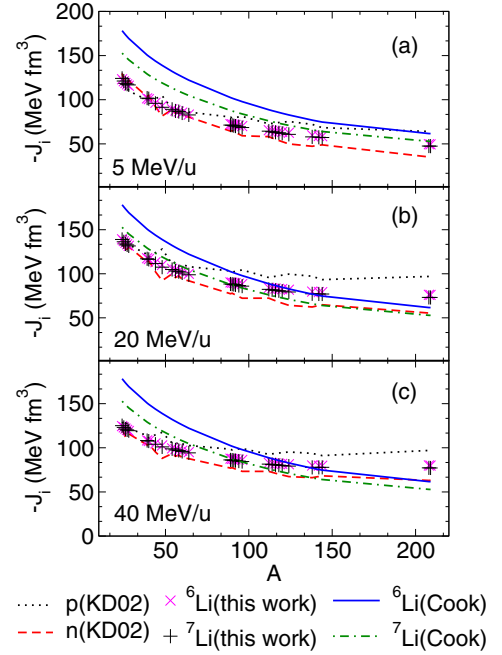


FIG. 5. Same as Fig. 4 but for imaginary part.

exhibit significant variations with respect to the target nucleus mass number, whereas the imaginary part of the volume integral per nucleon decreases evidently as the target nucleus mass number increases.

## IV. EXAMINATION OF PRESENT SYSTEMATIC OPTICAL POTENTIAL

### A. Elastic scattering angular distribution

To check the validity of our present systematic optical potential, we first calculated the elastic scattering angular distribution for $^6$Li and $^7$Li using our current systematic potential with the renormalization factors obtained from Eqs. (8) and (9), respectively. We also performed calculations using Cook's potential [35] for comparison. Figures 6–12 present these results in detail. The circles in the figures represent experimental data, while the solid and dashed lines are the calculated results using our present optical potential and Cook's, respectively. Here, we use hollow circles to represent data points where the ratio of the elastic scattering cross section to the Rutherford scattering cross section is less than 1%. We consider these points to be of less significance in theoretical analysis compared to the solid circles, which have a ratio greater than 1%.

The elastic scattering angular distributions of $^6$Li were computed for various targets and incident energies range. Specifically, the scattering of $^6$Li at 34 MeV was computed for $^{25,26}$Mg, $^{27}$Al, $^{28}$Si, $^{39}$K, $^{58}$Ni, $^{90,91}$Zr, and $^{209}$Bi targets, and the elastic scattering angular distributions for incident energies ranging from 35 to 39 MeV were calculated for targets $^{26}$Mg, $^{39}$K, $^{112,116}$Sn, $^{208}$Pb, and $^{209}$Bi. The computed results, along with relevant experimental data, are compared in Figs. 6(a) and 6(b), respectively. Both Cook's optical potential and our systematic optical potential can reproduce the
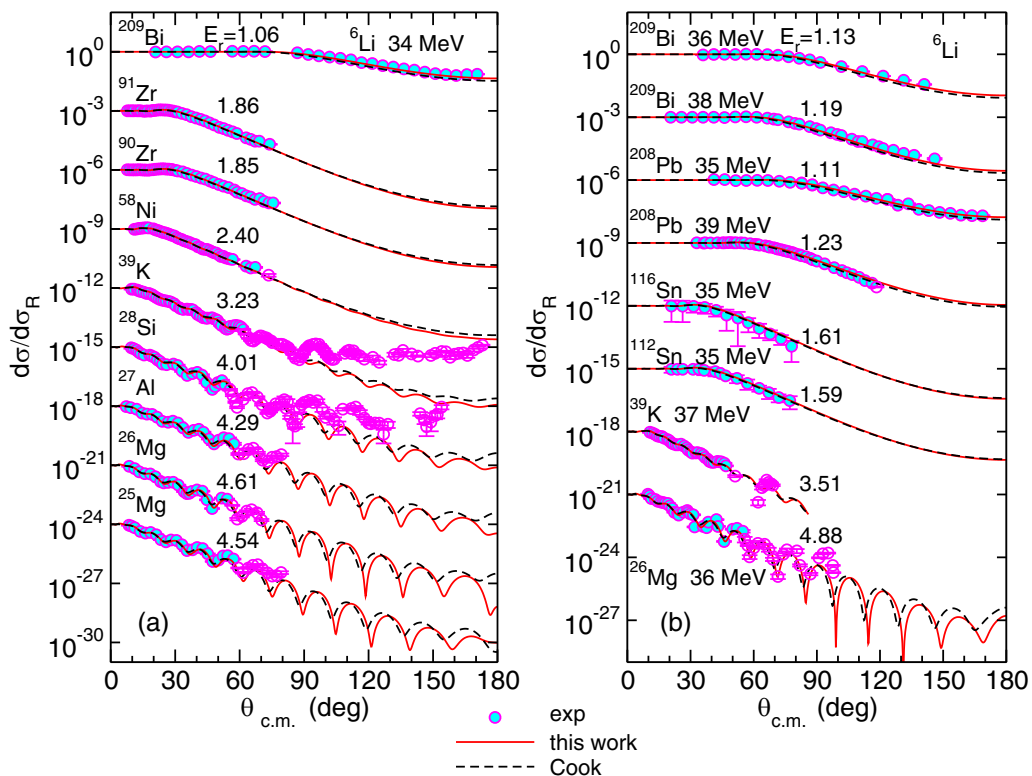
of our current systematic optical potential is the same as the KD02 optical potential but the magnitude of the volume integral per nucleon in our current potential is noticeably smaller than that of the neutron and proton potentials due to the adjustments made to the real part of the single-folding model potential. Second, as observed with Cook's systematic optical potential, the real part of the volume integral per nucleon of our systematic optical potential also decreases with increasing target mass number. However, it consistently has a smaller magnitude than Cook's.

Figure 5 displays the imaginary part of volume integrals per nucleon. To start with, our study showcases the volume integrals per nucleon of our optical potential for $^6$Li and $^7$Li exhibiting similar magnitudes and trends as reported by KD02 and Cook's optical potentials. The mass number of the target increases, the imaginary part of the volume integrals per nucleon of our optical potential for $^6$Li and $^7$Li decreases. However, compared to Cook's optical potential, this declining trend in our optical potential occurs at a slower rate. Moreover, when the incident energy increases, the imaginary part of the volume integral per nucleon of our optical potential is larger than that of Cook's optical potential in regions with large mass numbers of target nuclei.

Figures 4 and 5 also demonstrate that the real part of the volume integral per nucleon of the optical potential does not

FIG. 6. Elastic scattering angular distributions divided by Rutherford scattering angular distributions of $^6$Li scattering from various targets at incident energies indicated in the figures. The circles represent the experimental data, while the solid and dashed lines exhibit the calculated results with present systematic optical potential and Cook's, respectively. Different data sets are offset by factors of $10^{-3}$ for an optimal view. The hollow circles represent data points where the ratio of the elastic scattering cross section to the Rutherford scattering cross section is less than 1%. On the other hand, the solid circles represent data points with a ratio larger than 1%.
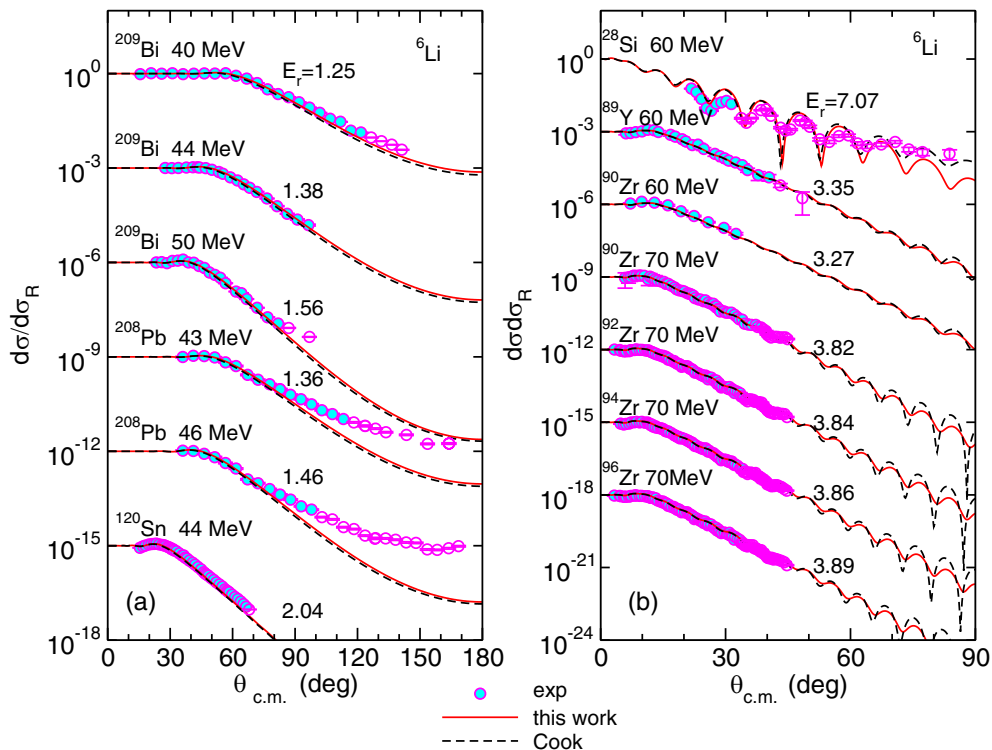


FIG. 7. Same as Fig. 6 but at different incident energies and for different targets.
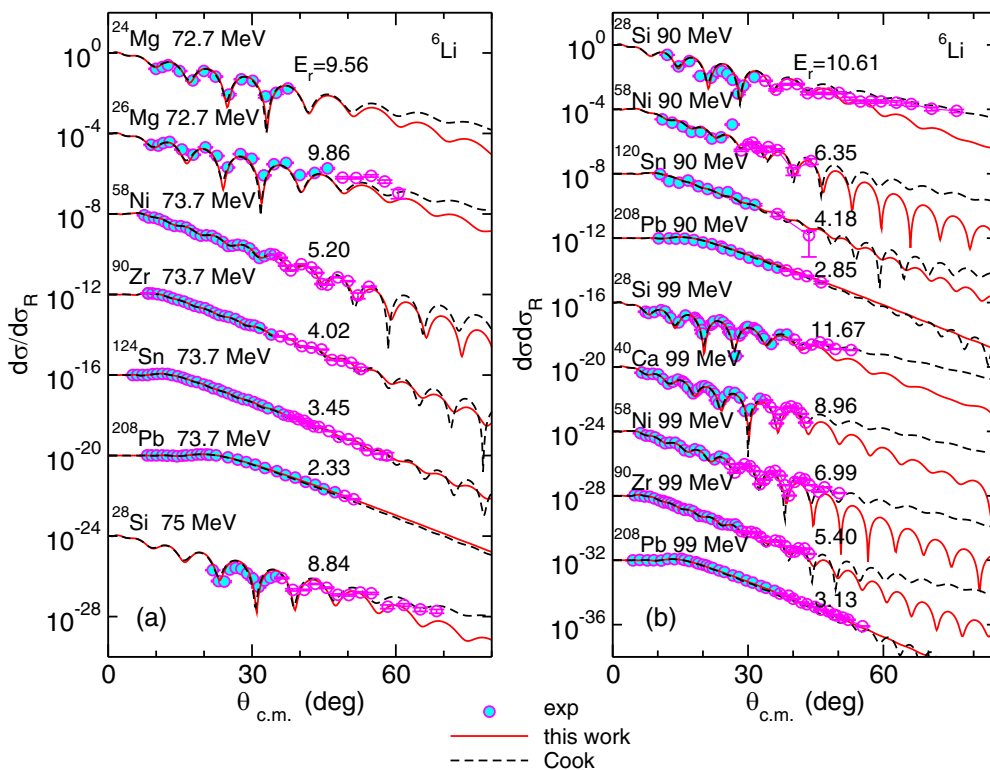
FIG. 8. Same as Fig. 6 but at different incident energies and for different targets. Different data set are offset by factors of $10^{-4}$ for optimum view.
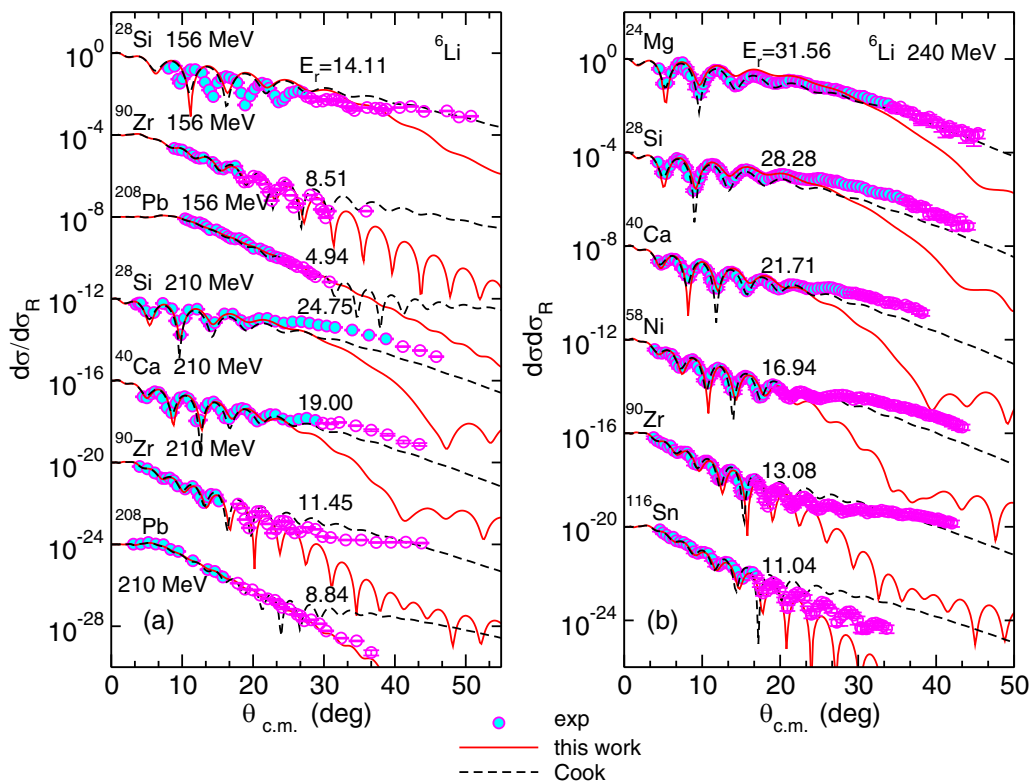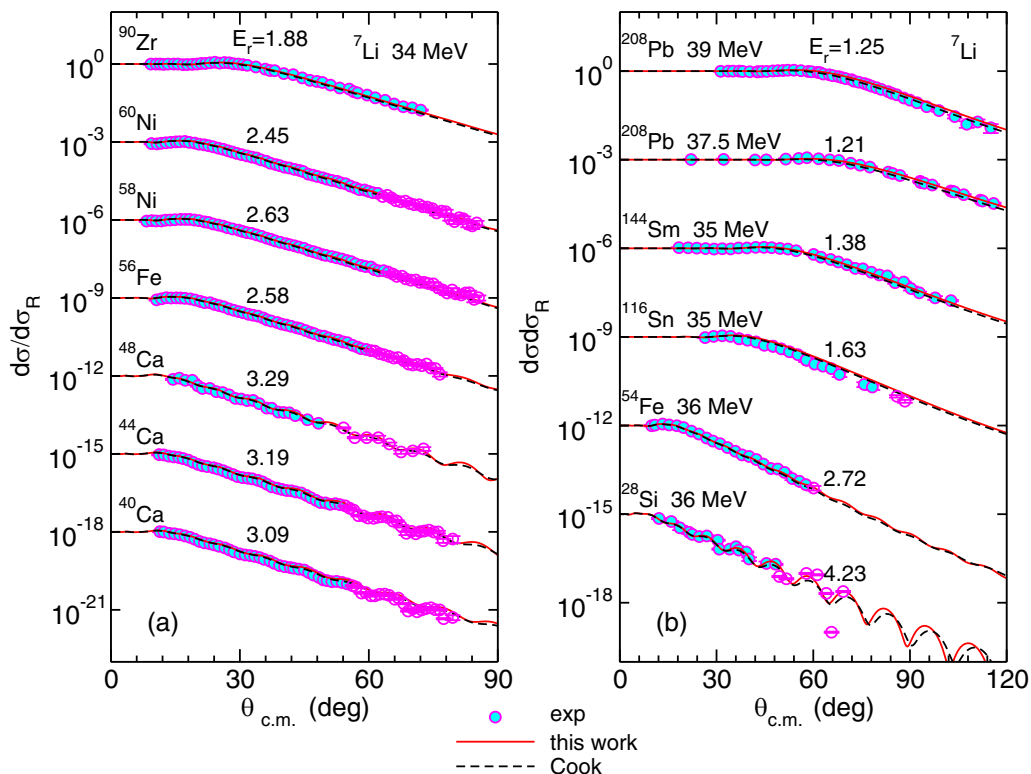


FIG. 9. Same as Fig. 6 but at different incident energies and for different targets. Different data set are offset by factors of $10^{-4}$ for optimum view.

FIG. 10. Elastic scattering angular distributions of $^7$Li scattering from various targets at incident energies indicated in the figures. The circles represents experimental data. The solid and dashed lines were calculated with present systematic optical potential and Cook's, respectively. Different data set are offset by factors of $10^{-3}$ for optimum view. The hollow circles represent data points where the ratio of the elastic scattering cross section to the Rutherford scattering cross section is less than 1%. On the other hand, the solid circles represent data points with a ratio larger than 1%.
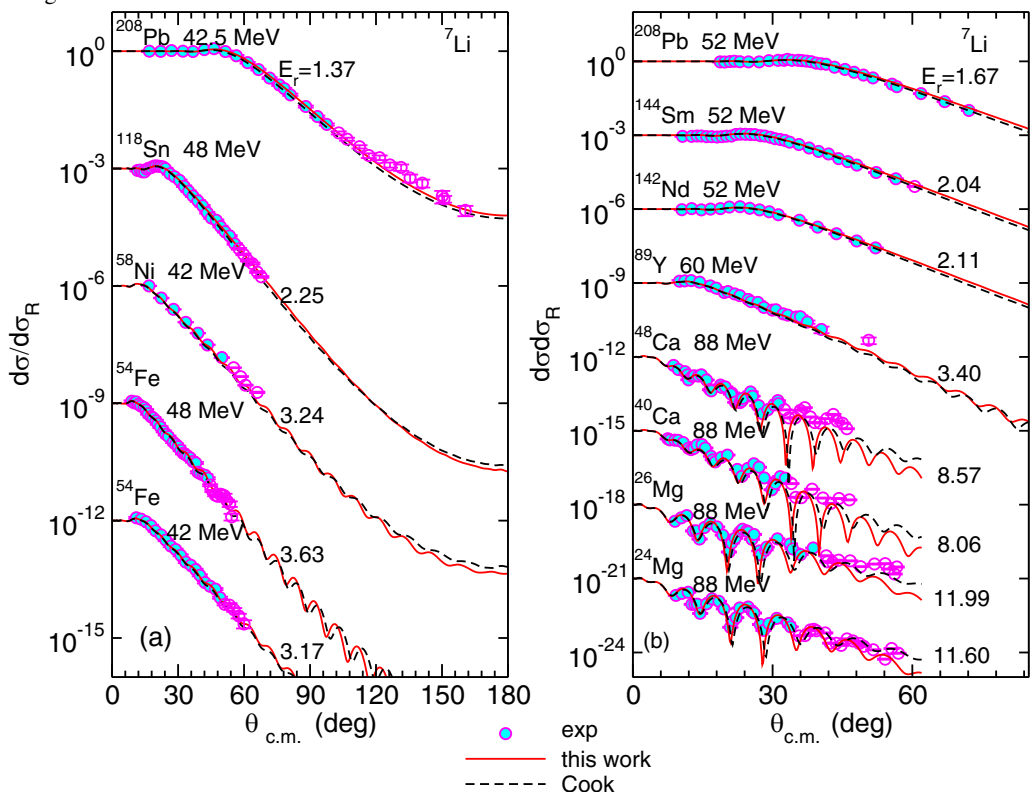


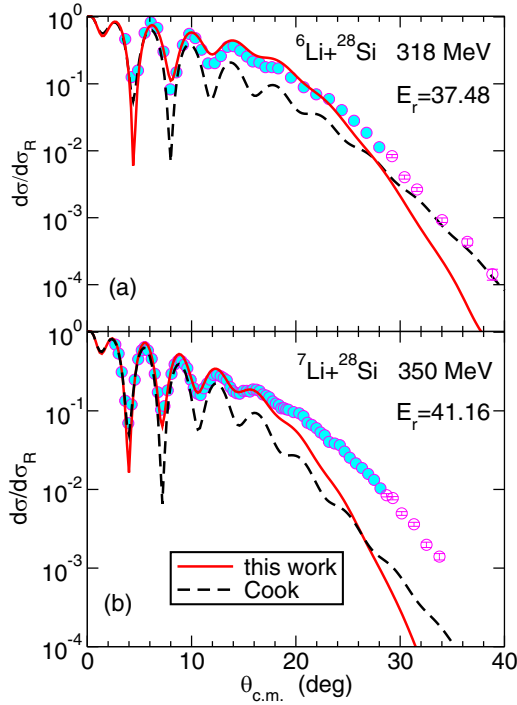FIG. 11. Same as Fig. 10 but at different incident energies and for different targets.

FIG. 12. (a) Elastic scattering angular distributions divided by Rutherford scattering angular distributions of $^6$Li scattering from $^{28}$Si at incident energy 318 MeV. (b) Elastic scattering angular distributions divided by Rutherford scattering angular distributions of $^7$Li scattering from $^{28}$Si at incident energy 350 MeV. The symbols represent the experimental data, while the solid and dashed lines exhibit the calculated results with present systematic optical potential and Cook's, respectively. The hollow circles represent data points where the ratio of the elastic scattering cross section to the Rutherford scattering cross section is less than 1%. On the other hand, the solid circles represent data points with a ratio larger than 1%.

experimental elastic scattering data with very similar results. However, for targets $^{28}$Si and $^{39}$K at an incident energy of 34 MeV, the experimental data extends beyond 90 degrees in the backward angle area, and neither our systematic optical potential nor Cook's systematic optical potential accurately predict these data points. Further investigation is required since the experimental data falls outside the limits of the systematics. The observed discrepancy may be explained by coupled-channel effects.

Figure 7(a) shows the elastic scattering angular distributions of $^6$Li with targets $^{120}$Sn, $^{208}$Pb, and $^{209}$Bi at energy ranges of 40–50 MeV, while Fig. 7(b) displays the elastic scattering angular distributions for targets $^{28}$Si, $^{89}$Y, and $^{90,92,94,96}$Zr at incident energies of 60 and 70 MeV. In most cases, the calculated results using our systematic optical potential and Cook's both are very similar and agreed well with the experimental data for all angular range except for target $^{208}$Pb at incident energies of 43 and 46 MeV beyond 70°, where both the current systematical OMP and Cook's calculations failed to accurately reproduce the experimental data.

We also analyzed the elastic scattering angular distributions of $^6$Li colliding with various targets at the incident

energy of 72.7, 73.7, 75, 90, and 99 MeV. Specifically, Fig. 8(a) displays the calculated results and experimental data at incident energies of 72.7, 73.7, and 75 MeV, while Fig. 8(b) displays the calculated results and experimental data at incident energies of 90 and 99 MeV. Again, the results obtained by our systematic optical potential and Cook's agree well with the experimental data within the angular range of interest. However, in the backward angles where no experimental data exists for some of the $^6$Li scattering systems, the results acquired from our systematic potential and Cook's model show apparent differences. Specifically, these systems include $^6$Li + $^{24,26}$Mg at an incident energy of 72.7 MeV, $^6$Li + $^{28}$Si at incident energies of 75, 90, and 99 MeV, $^6$Li + $^{40}$Ca at an incident energy of 99 MeV, $^6$Li + $^{58}$Ni at incident energies of 73.7, 90, and 99 MeV, and $^6$Li + $^{90}$Zr at an incident energy of 99 MeV.

At high energies ranging from 156, 210, to 240 MeV, the elastic scattering angular distributions of $^6$Li with different targets are presented in Fig. 9. At an incident energy of 156 MeV, the results obtained using our systematic optical potential and Cook's potential demonstrate good agreement with the experimental data, except for the $^6$Li + $^{28}$Si system, which shows a phase mismatch. When considering an incident energy of 210 MeV, our systematic optical potential and Cook's potential also show good agreement with the experimental data in forward angles for the $^{28}$Si, $^{40}$Ca, and $^{90}$Zr targets. For large angles, specifically when the ratio of the elastic scattering cross section to the Rutherford scattering cross section is less than 1%, neither our systematic optical potential nor Cook's potential properly captures these data points. In this region, the interference between the Coulomb force and the nuclear force is relatively weak, resulting in a relatively small contribution to theoretical analysis. For the $^{208}$Pb target at the same energy, our systematic potential reproduces the experimental data well, while Cook's potential fails to correctly reproduce the experimental data. In addition, at an incident energy of 240 MeV, both our systematic optical potential and Cook's potential exhibit good agreement with the experimental data in the region where the ratio of the elastic scattering cross section to the Rutherford scattering cross section is greater than 1%. This region is characterized by the dominance and importance of the interference between the Coulomb and nuclear forces in our theoretical analyses.

The elastic scattering angular distributions of $^7$Li were computed at different energies and target nuclei. Figure 10(a) shows the distributions for targets $^{40,44,48}$Ca, $^{56}$Fe, $^{58,60}$Ni, and $^{90}$Zr at an incident energy of 34 MeV. On the other hand, Fig. 10(b) illustrates the angular distributions for targets $^{28}$Si, $^{54}$Fe, $^{116}$Sn, $^{144}$Sm, and $^{208}$Pb at incident energies ranging from 35 to 39 MeV. Both Cook's and our systematic optical potential yielded comparable outcomes to the experimental elastic scattering data.

We also calculated the elastic scattering angular distributions of $^7$Li for various targets within an energy range of 40–48 MeV, including $^{54}$Fe, $^{58}$Ni, $^{118}$Sn, and $^{208}$Pb. Furthermore, we computed the elastic scattering angular distributions of $^7$Li for targets $^{24,26}$Mg, $^{44,48}$Ca, $^{89}$Y, $^{142}$Nd, and $^{144}$Sm, and $^{208}$Pb, at incident energies of 52, 60, and 88 MeV. We compared our results with the relevant experimental data and
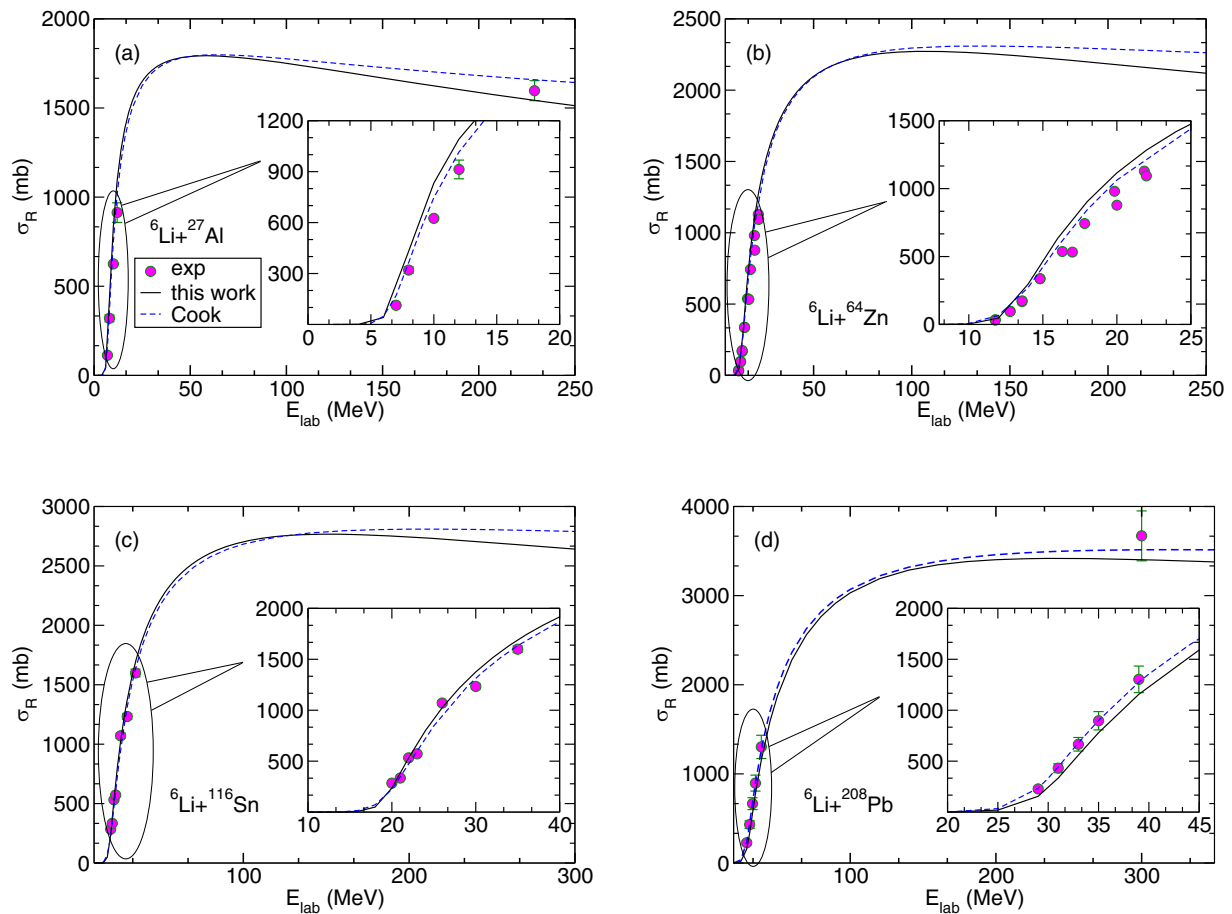
FIG. 13. Reaction cross sections as a function of incident energies for projectile $^6$Li. The target nuclei are indicated in the figure. The symbols represent the experimental data, the solid line represents the calculated results using our present systematic optical potential, and the dashed line represents the results calculated using Cook's optical potential. The experimental data are obtained from Refs. [51,61,72–76].

illustrated them in Fig. 11. The results obtained from Cook's and our optical potential give very similar results and are within good agreement with experimental data, except for incident energy of 88 MeV, where $E_r$ exceeds 5, calculated results obtained by our systematic potential and Cook's begin to show some differences.

Figures 12(a) and 12(b) demonstrate the elastic scattering angular distributions of $^6$Li + $^{28}$Si and $^7$Li + $^{28}$Si at higher incident energies of 318 and 350 MeV, respectively. The shape of the angular distribution of the experimental data is well reproduced by both Cook's and our systematic optical potential. Nevertheless, our systematic optical potential produced more accurate calculation results than Cook's in forward angles. Cook's optical potential showed better performance in the tail region of the angular distribution. However, the experimental data in this area is negligible, approximately less than 0.01.

## B. Reaction cross section

The reaction cross section is a crucial observable in the optical model, frequently utilized in testing nuclear models and gaining insights into the matter distribution of the projectile, as well as providing indications about its structure [80]. Researchers have shown significant interest in this data over

the years. Precise measurements of an elastic scattering can establish a suitable set of optical potential parameters corresponding to a specific system. Using these optical potential parameters, we can predict reaction cross sections for this system. As a result, reaction cross sections can serve as essential constraints in phenomenological optical model analyses [79]. Therefore, we used these data to validate our systematic potentials.

Figure 13 displays the reaction cross section of $^6$Li as a function of the incident energy in the laboratory frame for various target nuclei. The experimental data are represented by circles, while the calculated results using our optical potential and Cook's optical potential use solid and dashed lines, respectively. In order to clearly demonstrate the calculation results near the Coulomb barrier, we have included detailed subgraphs in each figure. In panel (a), experimental data around the Coulomb barrier were obtained from optical model fits conducted at four different energies [72]. Our calculated results effectively reproduce the trend of the cross section, dependent on the energy, and show good agreement with the magnitude of the experimental data. Conversely, only one experimental data point was available above 200 MeV [73]. The experimental data are in the middle of the results obtained by our systematic potential and Cook's potential.
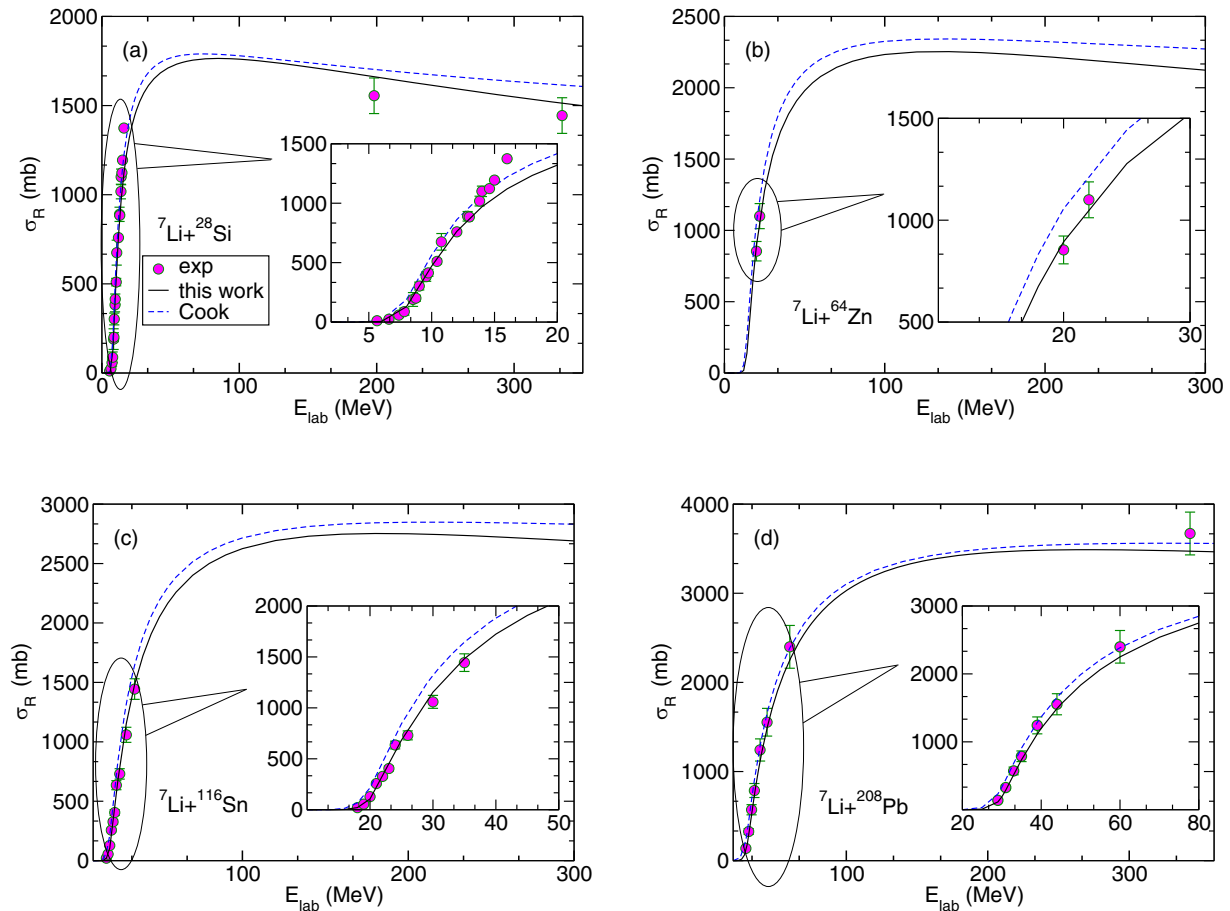
FIG. 14. Same as Fig. 13 but for $^7$Li. The experimental data are obtained from Refs. [51,61,75–79].

Panel (b) presents reaction cross section data for $^{64}$Zn taken from Refs. [74,75], and the calculated results still slightly exceed these data. In panel (c), only the reaction cross section extracted from elastic scattering data of $^6$Li $+ ^{116}$Sn were available [61], and our computations match well with the extracted data. Finally, panel (d) shows reaction cross sections near the Coulomb barrier for $^{208}$Pb taken from Ref. [51]. The computed results obtained using Cook's potential and our single folding potential are in agreement with the experimental data. Additionally, at 298 MeV, the reaction cross sections on $^{nat}$Pb were measured [76], and the results obtained using both our optical potential and Cook's optical potential underestimate the experimental value. In general, the comparison between the reaction cross section computed using our single folding potential and the experimental data is not as good as the results obtained using Cook's potential. This is mainly due to the averaging of the potential parameters over the entire energy range during the fitting process. Locally, in the energy region around the Coulomb barrier, the fitting is not an optimal solution, as shown in Fig. 2(a).

Figure 14 illustrates the reaction cross sections of $^7$Li for different target nuclei. Panel (a) presents the calculated reaction cross sections for $^{28}$Si using our systematic single potential for $^7$Li and Cook's potential, alongside the corresponding

experimental data [77–79]. The results obtained from our single potential agree well with the experimental data. At high energies, our single potential results better reflect the experimental data than Cook's potential. Panel (b) displays the reaction cross sections for $^{64}$Zn with only experimental data available at incident energies of 20 and 22 MeV [75]. Our computed results using the systematic potential align well with the experimental data, whereas the results obtained from Cook's potential overestimate these data. In panel (c), the reaction cross sections for $^{116}$Sn were calculated using our current single potential and compared with the experimental data [61]. Similarly, our computed results using the systematic single folding potential align well with the experimental data, while Cook's potential overestimates these data. Panel (d) presents the comparison of the reaction cross sections near the Coulomb barrier for $^{208}$Pb using our systematic potential and Cook's potential, with the corresponding experimental data from [51]. The experimental data can be effectively reproduced by our single folding potential and Cook's potential. For the $^7$Li $+ ^{208}$Pb system, high energy data [79] are available and have been compared with the cross sections computed using our single folding potential and Cook's potential. Both sets of results effectively reproduce the experimental data within the experimental uncertainties.

## V. CONCLUSION

We developed a new energy-dependent systematic optical potential for $^6$Li and $^7$Li based on the KD02 optical potential within the framework of the single-folding model. The single-folding model potential required only one free parameter for renormalization purposes, and the renormalization factors were obtained by fitting experimental elastic-scattering angular distributions for target nuclei with masses ranging from 24 to 209 at incident energies lower than 350 MeV, exhibiting a good linear trend. Overall, our systematic optical potential provides comparably predictive capabilities to the systematic optical potential proposed by Cook [35], except for light target nuclei at high energy where experimental data have shown a high sensitivity to the inner portion of the optical model potentials [81].

The single-folding model can be extended to other types of projectiles. Therefore, calculations were conducted on $^{12}$C and $^{16}$O nuclei, which yielded fitted $N_r$ values of approximately 0.5. However, the scarcity of experimental data in high-energy regions has hindered the detection of clear patterns in $N_r$. With the accumulation of more experimental data for heavier nuclei at high energies, it may become feasible to establish a systematic optical potential for these nuclei in a similar way. Interestingly, $^{12}$C and $^{16}$O are tightly bound nuclei with significantly different properties from $^6$Li and $^7$Li, but the difference in their renormalization factors is minimal. Further efforts should be made to investigate the similarities and differences in the renormalization factors among different projectiles.

The introduction of this novel single folding potential provides a potential solution to minimize systematic errors in distorted wave calculations, such as transfer and inclusive breakup. Specifically, all potentials utilized in the calculations are derived from the commonly employed KD02 global potential.

[1] J. Lei and A. M. Moro, Phys. Rev. C **92**, 044616 (2015).

[2] J. Lei and A. M. Moro, Phys. Rev. C **92**, 061602(R) (2015).

[3] J. Lei and A. M. Moro, Phys. Rev. C **95**, 044605 (2017).

[4] N. Austerm, *Direct Nuclear Reaction Theories* (Wiley, New York, 1970).

[5] N. K. Glendenning, *Direct Nuclear Reactions* (World Scientific Publishing Co., River Edge, NJ, 2004).

[6] G. R. Satchler, *Direct Nuclear Reactions* (Oxford University Press, New York, 1983).

[7] F. G. Perey, Phys. Rev. **131**, 745 (1963).

[8] F. D. Becchetti and G. W. Greenlees, Phys. Rev. **182**, 1190 (1969).

[9] P. E. Hodgson, Rep. Prog. Phys. **47**, 613 (1984).

[10] R. Varner, W. Thompson, T. McAbee, E. Ludwig, and T. Clegg, Phys. Rep. **201**, 57 (1991).

[11] A. Koning and J. Delaroche, Nucl. Phys. A **713**, 231 (2003).

[12] W. W. Daehnick, J. D. Childs, and Z. Vrcelj, Phys. Rev. C **21**, 2253 (1980).

[13] D. Y. Pang, P. Roussel-Chomaz, H. Savajols, R. L. Varner, and R. Wolski, Phys. Rev. C **79**, 024615 (2009).

[14] D. Y. Pang, Y. L. Ye, and F. R. Xu, Phys. Rev. C **83**, 064619 (2011).

[15] X. Li, C. Liang, and C. Cai, Nucl. Phys. A **789**, 103 (2007).

[16] J. Cook, Nucl. Phys. A **388**, 153 (1982).

[17] V. A. B. Zagatto, B. R. Gonçalves, and D. R. Mendes Junior, Phys. Rev. C **107**, 044604 (2023).

[18] Y. Xu, Y. Han, J. Hu, H. Liang, Z. Wu, H. Guo, and C. Cai, Phys. Rev. C **98**, 024619 (2018).

[19] Y. Xu, Y. Han, J. Hu, H. Liang, Z. Wu, H. Guo, and C. Cai, Phys. Rev. C **97**, 014615 (2018).

[20] J. Lei and A. M. Moro, Advancing the IAV model with CDCC wave functions for realistic descriptions of two-body projectile breakup, arXiv:2305.14111.

[21] J. Liu, J. Lei, and Z. Ren, Testing the validity of the surface approximation for reactions induced by weekly bound nuclei with a fully quantum-mechanical model, Phys. Rev. C **108**, 024606 (2023).

[22] D. Jackson and R. Johnson, Phys. Lett. B **49**, 249 (1974).

[23] Y. P. Xu and D. Y. Pang, Phys. Rev. C **87**, 044605 (2013).

[24] Y. Sakuragi, M. Yahiro, and M. Kamimura, Prog. Theor. Phys. Suppl. **89**, 136 (1986).

[25] G. Satchler, Phys. Rep. **199**, 147 (1991).

[26] M. Brandan and G. Satchler, Phys. Rep. **285**, 143 (1997).

[27] R. Bass, *Nuclear Reactions with Heavy Ions* (Springer, New York, 1980).

[28] G. A. Lalazissis, T. Nikšić, D. Vretenar, and P. Ring, Phys. Rev. C **71**, 024312 (2005).

[29] F. Petrovich, D. Stanley, L. A. Parks, and P. Nagel, Phys. Rev. C **17**, 1642 (1978).

[30] D. Perkin, A. Kobos, and J. Rook, Nucl. Phys. A **245**, 343 (1975).

[31] A. Bonaccorso and F. Carstoiu, Nucl. Phys. A **706**, 322 (2002).

[32] V. V. Parkar, V. Jha, B. J. Roy, S. Santra, K. Ramachandran, A. Shrivastava, A. Chatterjee, S. R. Jain, A. K. Jain, and S. Kailas, Phys. Rev. C **78**, 021601(R) (2008).

[33] N. Otuka, E. Dupont, V. Semkova, B. Pritychenko, A. I. Blokhin, M. Aikawa, S. Babykina, M. Bossant, G. Chen, S. Dunaeva, R. A. Forrest, T. Fukahori, N. Furutachi, S. Ganesan, Z. Ge, O. O. Gritzay, M. Herman, S. Hlavač, K. Katō, B. Lalremruata *et al.*, Nuclear Data Sheets **120**, 272 (2014).

[34] P. Schwandt, W. W. Jacobs, M. D. Kaitchuck, P. P. Singh, W. D. Ploughe, F. D. Becchetti, and J. Jänecke, Phys. Rev. C **24**, 1522 (1981).

[35] J. Cook, H. Gils, H. Rebel, Z. Majka, and H. Klewe-Nebenius, Nucl. Phys. A **388**, 173 (1982).

[36] P. Clark, T. Ophel, J. Nurzynski, C. Atwood, and D. Hebbard, Nucl. Phys. A **352**, 267 (1981).

[37] M. F. Steeden, J. Coopersmith, S. J. Cartwright, M. D. Cohler, N. M. Clarke, and R. J. Griffiths, J. Phys. G **6**, 501 (1980).

[38] T. Tanabe, K. Haga, M. Yasue, K. Sato, K. Ogino, Y. Kadota, M. Tochi, K. Makino, T. Kitahara, and T. Shiba, Nucl. Phys. A **399**, 241 (1983).

[39] R. Puigh and K. Kemper, Nucl. Phys. A **313**, 363 (1979).

[40] X. Chen, Y. W. Lui, H. L. Clark, Y. Tokimoto, and D. H. Youngblood, Phys. Rev. C **80**, 014312 (2009).

[41] D. J. Horen, R. L. Auble, J. Gomez del Campo, G. R. Satchler, R. L. Varner, J. R. Beene, B. Lund, V. R. Brown, P. L. Anthony, and V. A. Madsen, Phys. Rev. C **47**, 629 (1993).

[42] G. Ciangaru, R. McGrath, and F. Cecil, Nucl. Phys. A **380**, 147 (1982).

[43] P. Schumacher, N. Ueta, H. Duhm, K.-I. Kubo, and W. Klages, Nucl. Phys. A **212**, 573 (1973).

[44] N. N. Deshmukh, S. Mukherjee, D. Patel, N. L. Singh, P. K. Rath, B. K. Nayak, D. C. Biswas, S. Santra, E. T. Mirgule, L. S. Danu, Y. K. Gupta, A. Saxena, R. K. Choudhury, R. Kumar, J. Lubian, C. C. Lopes, E. N. Cardozo, and P. R. S. Gomes, Phys. Rev. C **83**, 024607 (2011).

[45] M. Vineyard, J. Cook, and K. Kemper, Nucl. Phys. A **405**, 429 (1983).

[46] K. Becker, K. Blatt, H. Jänsch, W. Korsch, H. Leucker, W. Luck, H. Reich, H.-G. Völk, D. Fick, and K. Rusek, Nucl. Phys. A **535**, 189 (1991).

[47] Yu. A. Glukhov, A. S. Dem'yanova, S. I. Drozdov, M. V. Zhukov, V. I. Man'ko, B. G. Novatskii, A. A. Ogloblin, S. B. Sakuta, D. N. Stepanov, and L. V. Chulkov, Yad. Fiz. **34**, 312 (1981).

[48] Y. A. Glukhov, A. S. Dem'yanova, V. I. Man'ko, B. G. Novatskij, A. A. Ogloblin, S. B. Sakuta, D. N. Stepanov, and V. I. Chuev, Rept Inst. Atomnoy Energii, Kurchatov Reports, No. 2989 (1978), https://www-nds.iaea.org/exfor//servlet/X4sDownloadPdf?x4ref=R,IAE-2989,1978&x4codin=3.

[49] R. Huffman, A. Galonsky, R. Markham, and C. Williamson, Phys. Rev. C **22**, 1522 (1980).

[50] Z. Chun-Lei, Z. Huan-Qiao, L. Cheng-Jian, R. Ming, L. Zu-Hua, Y. Feng, W. Xiu-Kun, Z. Ping, A. Guang-Peng, J. Hui-Ming, W. Zhen-Dong, X. Xin-Xing, and B. Chun-Lin, Chin. Phys. Lett. **23**, 1146 (2006).

[51] N. Keeley, S. Bennett, N. Clarke, B. Fulton, G. Tungate, P. Drumm, M. Nagarajan, and J. Lilley, Nucl. Phys. A **571**, 326 (1994).

[52] A. Nadasen, M. McMaster, M. Fingal, J. Tavormina, P. Schwandt, J. S. Winfield, M. F. Mohar, F. D. Becchetti, J. W. Jänecke, and R. E. Warner, Phys. Rev. C **39**, 536 (1989).

[53] J. Szymakowski, K. Kemper, and A. Frawley, Nucl. Phys. A **355**, 221 (1981).

[54] Krishichayan, X. Chen, Y.-W. Lui, J. Button, and D. H. Youngblood, Phys. Rev. C **81**, 044612 (2010).

[55] K. D. Veal, C. R. Brune, W. H. Geist, H. J. Karwowski, E. J. Ludwig, E. E. Bartosz, P. D. Cathers, T. L. Drummer, K. W. Kemper, A. M. Eiró, F. D. Santos, B. Kozlowska, H. J. Maier, and I. J. Thompson, Phys. Rev. C **60**, 064003 (1999).

[56] S. Santra, S. Kailas, K. Ramachandran, V. V. Parkar, V. Jha, B. J. Roy, and P. Shukla, Phys. Rev. C **83**, 034616 (2011).

[57] R. Wadsworth, M. D. Cohler, M. J. Smithson, D. L. Watson, F. Jundt, L. Kraus, I. Linck, and J. C. Sens, J. Phys. G **9**, 1237 (1983).

[58] A. Nadasen, J. Brusoe, J. Farhat, T. Stevens, J. Williams, L. Nieman, J. S. Winfield, R. E. Warner, F. D. Becchetti, J. W. Jänecke, T. Annakkage, J. Bajema, D. Roberts, and H. S. Govinden, Phys. Rev. C **52**, 1894 (1995).

[59] C. Glover, R. Cutler, and K. Kemper, Nucl. Phys. A **341**, 137 (1980).

[60] D. Gupta, C. Samanta, R. Kanungo, M. Sharan, S. Kailas, A. Chatterjee, K. Mahata, and A. Shrivastava, Nucl. Phys. A **646**, 161 (1999).

[61] N. N. Deshmukh, S. Mukherjee, B. K. Nayak, D. C. Biswas, S. Santra, E. T. Mirgule, S. Appannababu, D. Patel, A. Saxena, R. K. Choudhury, J. Lubian, and P. R. S. Gomes, Eur. Phys. J. A **47**, 118 (2011).

[62] J. M. Figueira, J. O. Fernandez Niello, A. Arazi, O. A. Capurro, P. Carnelli, L. Fimiani, G. V. Martí, D. Martinez Heimann, A. E. Negri, A. J. Pacheco, J. Lubian, D. S. Monteiro, and P. R. S. Gomes, Phys. Rev. C **81**, 024613 (2010).

[63] L. Yang, C. J. Lin, H. M. Jia, F. Yang, Z. D. Wu, X. X. Xu, H. Q. Zhang, Z. H. Liu, P. F. Bao, L. J. Sun, and N. R. Ma, Phys. Rev. C **89**, 044615 (2014).

[64] I. J. Thompson, Comput. Phys. Rep. **7**, 167 (1988).

[65] F. James and M. Roos, Comput. Phys. Commun. **10**, 343 (1975).

[66] G. Igo, Phys. Rev. Lett. **1**, 72 (1958).

[67] G. Satchler and W. Love, Phys. Rep. **55**, 183 (1979).

[68] M. Matoba, M. Hyakutake, and I. Kumabe, Phys. Rev. C **32**, 1773 (1985).

[69] G. W. Greenlees, G. J. Pyle, and Y. C. Tang, Phys. Rev. **171**, 1115 (1968).

[70] D. C. Agrawal and P. C. Sood, Phys. Rev. C **11**, 1854 (1975).

[71] P. Hodgson, Phys. Lett. B **65**, 331 (1976).

[72] E. Benjamim, A. Lépine-Szily, D. Mendes Junior, R. Lichtenthäler, V. Guimarães, P. Gomes, L. Chamon, M. Hussein, A. Moro, A. Arazi, I. Padron, J. Alcantara Nuñez, M. Assunção, A. Barioni, O. Camargo, R. Denke, P. de Faria, and K. Pires, Phys. Lett. B **647**, 30 (2007).

[73] M. Fukuda, M. Mihara, T. Fukao, S. Fukuda, M. Ishihara, S. Ito, T. Kobayashi, K. Matsuta, T. Minamisono, S. Momota, T. Nakamura, Y. Nojiri, Y. Ogawa, T. Ohtsubo, T. Onishi, A. Ozawa, T. Suzuki, M. Tanigaki, I. Tanihata, and K. Yoshida, Nucl. Phys. A **656**, 209 (1999).

[74] M. Zadro, P. Figuera, A. Di Pietro, F. Amorini, M. Fisichella, O. Goryunov, M. Lattuada, C. Maiolino, A. Musumarra, V. Ostashko, M. Papa, M. G. Pellegriti, F. Rizzo, D. Santonocito, V. Scuderi, and D. Torresi, Phys. Rev. C **80**, 064610 (2009).

[75] P. R. S. Gomes, M. D. Rodríguez, G. V. Martí, I. Padron, L. C. Chamon, J. O. Fernández Niello, O. A. Capurro, A. J. Pacheco, J. E. Testoni, A. Arazi, M. Ramírez, R. M. Anjos, J. Lubian, R. Veiga, R. Liguori Neto, E. Crema, N. Added, C. Tenreiro, and M. S. Hussein, Phys. Rev. C **71**, 034608 (2005).

[76] R. E. Warner, M. H. McKinnon, N. C. Shaner, F. D. Becchetti, A. Nadasen, D. A. Roberts, J. A. Brown, A. Galonsky, J. J. Kolata, R. M. Ronningen, M. Steiner, and K. Subotic, Phys. Rev. C **62**, 024608 (2000).

[77] A. Pakou, K. Rusek, N. Alamanos, X. Aslanoglou, M. Kokkoris, A. Lagoyannis, T. J. Mertzimekis, A. Galonsky, N. G. Nicolis, D. Pierroutsakou, and D. Roubos, Eur. Phys. J. A **39**, 187 (2009).

[78] A. Musumarra, P. Figuera, F. De Luca, A. Di Pietro, P. Finocchiaro, M. Fisichella, M. Lattuada, A. Pakou, M. Pellegriti, G. Randisi, G. Scalia, C. Scirè, S. Scirè, V. Scuderi, D. Torresi, and M. Zadro, Nucl. Instrum. Methods Phys. Res. A **612**, 399 (2010).

[79] R. E. Warner, R. A. Patty, P. M. Voyles, A. Nadasen, F. D. Becchetti, J. A. Brown, H. Esbensen, A. Galonsky, J. J. Kolata, J. Kruse, M. Y. Lee, R. M. Ronningen, P. Schwandt, J. von Schwarzenberg, B. M. Sherrill, K. Subotic, J. Wang, and P. Zecher, Phys. Rev. C **54**, 1700 (1996).

[80] M. Hemalatha, N. Maladkar, and S. Kailas, Phys. Rev. C **92**, 024611 (2015).

[81] D. T. Khoa, W. von Oertzen, H. G. Bohlen, and S. Ohkubo, J. Phys. G: Nucl. Part. Phys. **34**, R111 (2007).